Accelerating convergence in orbital magnetization calculations through a single point formula and applications to defect EPR g-tensor fingerprints

S. Fioccola,[1,*] L. Giacomazzi,[2] D. Ceresoli,[3] N. Richard,[4] L. Martin-Samos,[2] and A. Hemeryck[1]

[1] *LAAS-CNRS, Université de Toulouse, CNRS, Toulouse, France*
[2] *CNR - Istituto Officina dei Materiali (IOM), c/o SISSA Via Bonomea 265, IT-34136 Trieste, Italy*
[3] *CNR-SCITEC – Istituto di Scienze e Tecnologie Chimiche "G. Natta", National Research Council of Italy, via C. Golgi 19, Milano 20133, Italy*
[4] *CEA, DAM, CESTA, F-33114 Le Barp, France*

SUPPLEMENTARY MATERIALS

Tables and Graphs

TABLE I. EPR g-tensor of the E-center (PV^0) in silicon as a function of supercell size, using Γ-point sampling. Results from linear response methods (QE-GIPAW and CASTEP) are compared with those from the converse method, using both the covariant derivative and the single-point formula. Columns "$|\text{dev}\%_{\text{exp}}|$" indicate the absolute relative deviation of each principal g component from the experimental values reported in the last row.

Method	**Supercell**	$\mathbf{g}_1$	$\mathbf{g}_2$	$\mathbf{g}_3$	$\lvert\text{dev}\%_{\text{exp}}\rvert\mathbf{g}_1$	$\lvert\text{dev}\%_{\text{exp}}\rvert$ $\mathbf{g}_2$	$\lvert\text{dev}\%_{\text{exp}}\rvert$ $\mathbf{g}_3$
QE-GIPAW	215-atom	1.9887	1.9959	1.9933	0.590	0.761	0.811
	511-atom	1.9937	1.9977	1.9979	0.340	0.671	0.582
	999-atom	-	-	-	-	-	-
CASTEP	215-atom	1.9888	1.9961	1.9947	0.585	0.751	0.741
	511-atom	1.9937	1.9977	1.9986	0.340	0.671	0.547
	999-atom	-	-	-	-	-	-
QE-CONVERSE (covariant)	215-atom	1.9971	2.0075	2.0052	0.170	0.184	0.219
	511-atom	1.9993	2.0084	2.0083	0.060	0.139	0.065
	999-atom	1.9998	2.0107	2.0086	0.035	0.025	0.050
QE-CONVERSE (single point)	215-atom	2.0025	2.0113	2.0078	0.100	0.005	0.090
	511-atom	2.0013	2.0110	2.0066	0.040	0.010	0.149
	999-atom	2.0005	2.0118	2.0077	0.000	0.030	0.095
Exp. [1]	-	**2.0005**	**2.0112**	**2.0096**	-	-	-

TABLE II. EPR g-tensor of the substitutional nitrogen defect in silicon (N_{Si}) as a function of supercell size, using Γ-point sampling. Results from linear response methods (QE-GIPAW and CASTEP) are compared with those from the converse method, using both the covariant derivative and the single-point formula. Columns "$|\text{dev}\%_{\text{exp}}|$" indicate the absolute relative deviation of each principal g component from the experimental values reported in the last row.

Method	**Supercell**	$\mathbf{g}_{\parallel}$	$\mathbf{g}_{\perp}$	$\lvert\text{dev}\%_{\text{exp}}\rvert$ $\mathbf{g}_{\parallel}$	$\lvert\text{dev}\%_{\text{exp}}\rvert$ $\mathbf{g}_{\perp}$
QE-GIPAW	216-atom	2.02125	2.03755	0.952	1.448
	512-atom	2.00972	2.02115	0.376	0.631
	1000-atom	-	-	-	-
CASTEP	216-atom	2.02492	2.04361	1.135	1.740
	512-atom	2.01123	2.02404	0.452	0.775
	1000-atom	-	-	-	-
QE-CONVERSE (covariant)	216-atom	1.99913	2.00914	0.153	0.033
	512-atom	2.00150	2.01016	0.034	0.084
	1000-atom	2.00180	2.01013	0.019	0.083
QE-CONVERSE (single point)	216-atom	2.00223	2.00862	0.002	0.007
	512-atom	2.00218	2.00904	0.0005	0.028
	1000-atom	2.00217	2.00905	0.001	0.029
Exp. [2]	-	**2.00219**	**2.00847**	—	

TABLE III. EPR g-tensor of the V^+ defect in silicon as a function of supercell size, using Γ-point sampling. Results from linear response methods (QE-GIPAW and CASTEP) are compared with those from the converse method, using both the covariant derivative and the single-point formula. Columns "|dev%$_{\text{exp}}$|" indicate the absolute relative deviation of each principal g component from the experimental values reported in the last row.

Method	**Supercell**	$\mathbf{g}_\parallel$	$\mathbf{g}_\perp$	|dev%$_{\text{exp}}$| $\mathbf{g}_\parallel$	|dev%$_{\text{exp}}$| $\mathbf{g}_\perp$
QE-GIPAW	215-atom	1.9983	1.9867	0.518	0.610
	511-atom	2.0009	1.9866	0.388	0.615
	999-atom	–	–	–	–
CASTEP	215-atom	1.9969	1.9869	0.587	0.600
	511-atom	2.0012	1.9855	0.373	0.670
	999-atom	–	–	–	–
QE-CONVERSE (covariant)	215-atom	2.0056	2.0026	0.154	0.185
	511-atom	2.0260	1.9926	0.861	0.313
	999-atom	2.0413	1.9530	1.623	2.296
QE-CONVERSE (single point)	215-atom	1.9830	1.9793	1.279	0.980
	511-atom	2.0008	1.9995	0.393	0.030
	999-atom	2.0076	1.9991	0.055	0.010
Exp. [3]	–	**2.0087**	**1.9989**	—	

TABLE IV. EPR g-tensor of the V^- defect in silicon as a function of supercell size, using Γ-point sampling. Results from linear response methods (QE-GIPAW and CASTEP) are compared with those from the converse method, using both the covariant derivative and the single-point formula. Columns "|dev%$_{\text{exp}}$|" indicate the absolute relative deviation of each principal g component from the experimental values reported in the last row.

Method	**Supercell**	$\mathbf{g_1}$	$\mathbf{g_2}$	$\mathbf{g_3}$	|dev%$_{\text{exp}}$|$\mathbf{g}_1$	|dev%$_{\text{exp}}$| $\mathbf{g}_2$	|dev%$_{\text{exp}}$| $\mathbf{g}_3$
QE-GIPAW	215-atom	1.9988	1.9962	1.9999	0.255	0.330	0.759
	511-atom	1.9972	1.9892	2.0001	0.334	0.679	0.744
	999-atom	–	–	–	–	–	–
CASTEP	215-atom	1.9987	1.9973	1.9993	0.260	0.275	0.784
	511-atom	1.9972	1.9882	2.0000	0.334	0.729	0.750
	999-atom	–	–	–	–	–	–
QE-CONVERSE (covariant)	215-atom	2.0017	2.0013	2.0036	0.110	0.075	0.571
	511-atom	2.0037	2.0029	2.0139	0.010	0.005	0.059
	999-atom	2.0033	2.0029	2.0156	0.030	0.005	0.025
QE-CONVERSE (single point)	215-atom	2.0065	1.9820	2.0158	0.130	1.039	0.035
	511-atom	2.0042	1.9972	2.0162	0.015	0.279	0.055
	999-atom	2.0034	1.9992	2.0161	0.025	0.180	0.050
Exp. [4]	–	**2.0039**	**2.0028**	**2.0151**	—		

TABLE V. EPR g-tensor of the SiV^0 / KUL1 defect in diamond as a function of supercell size, using Γ-point sampling. Results from linear response methods (QE-GIPAW and CASTEP) are compared with those from the converse method, using both the covariant derivative and the single-point formula. Columns "|dev%$_{\text{exp}}$|" indicate the absolute relative deviation of each principal g component from the experimental values reported in the last row.

Method	**Supercell**	$\mathbf{g}_\parallel$	$\mathbf{g}_\perp$	|dev%$_{\text{exp}}$| $\mathbf{g}_\parallel$	|dev%$_{\text{exp}}$| $\mathbf{g}_\perp$
QE-GIPAW	215-atom	2.0234	2.0195	0.963	0.799
	511-atom	2.0200	2.0146	0.793	0.554
	999-atom	2.0158	2.0113	0.584	0.390
CASTEP	215-atom	2.0231	2.0201	0.948	0.827
	511-atom	2.0203	2.0148	0.808	0.564
	999-atom	2.0160	2.0115	0.594	0.400
QE-CONVERSE (covariant)	215-atom	2.0127	2.0103	0.429	0.339
	511-atom	2.0105	2.0080	0.319	0.225
	999-atom	2.0083	2.0063	0.209	0.140
QE-CONVERSE (single point)	215-atom	2.0002	2.0015	0.195	0.100
	511-atom	2.0020	2.0026	0.105	0.045
	999-atom	2.0033	2.0034	0.040	0.005
Exp. [5]	–	**2.0041**	**2.0035**	—	

TABLE VI. Calculation of the g-tensor for the E_1' center in α-quartz silica as a function of supercell size, using Γ-point sampling. Results from linear response methods (QE-GIPAW and CASTEP) are compared with those from the converse method, using both the covariant derivative and the single-point formula. Columns "$|\mathrm{dev}\%_{\mathrm{exp}}|$" indicate the absolute relative deviation of each principal g component from the experimental values reported in the last row.

Method	**Supercell**	$\mathbf{g_1}$	$\mathbf{g_2}$	$\mathbf{g_3}$	$\lvert\mathrm{dev}\%_{\mathrm{exp}}\rvert\,\mathbf{g}_1$	$\lvert\mathrm{dev}\%_{\mathrm{exp}}\rvert\ \mathbf{g}_2$	$\lvert\mathrm{dev}\%_{\mathrm{exp}}\rvert\ \mathbf{g}_3$
QE-GIPAW	71-atom	2.00251	2.00109	2.00089	0.039	0.029	0.031
	161-atom	2.00191	2.00056	2.00048	0.009	0.002	0.011
	242-atom	2.00167	2.00046	2.00026	0.002	0.002	0.0005
	575-atom	2.00158	2.00035	2.00018	0.007	0.008	0.005
	1123-atom	–	–	–	–	–	–
CASTEP	71-atom	2.00274	2.00145	2.00122	0.051	0.047	0.047
	161-atom	2.00200	2.00075	2.00065	0.014	0.012	0.019
	242-atom	2.00173	2.00064	2.00042	0.0005	0.006	0.007
	575-atom	2.00163	2.00042	2.00023	0.004	0.004	0.002
	1123-atom	–	–	–	–	–	–
QE-CONVERSE (covariant)	71-atom	2.00176	2.00000	1.99959	0.002	0.025	0.034
	161-atom	2.00162	2.00015	2.00007	0.005	0.018	0.010
	242-atom	2.00161	2.00019	2.00009	0.005	0.016	0.009
	575-atom	2.00160	2.00028	2.00013	0.006	0.011	0.007
	1123-atom	2.00158	2.00027	2.00014	0.007	0.012	0.006
QE-CONVERSE (single point)	71-atom	2.00205	2.00024	1.99986	0.016	0.013	0.020
	161-atom	2.00190	2.00039	2.00034	0.009	0.006	0.003
	242-atom	2.00189	2.00043	2.00036	0.008	0.004	0.005
	575-atom	2.00188	2.00052	2.00039	0.008	0.0005	0.006
	1123-atom	2.00187	2.00051	2.00041	0.007	0.000	0.007
Exp. [6]	–	**2.00172**	**2.00051**	**2.00027**	—		

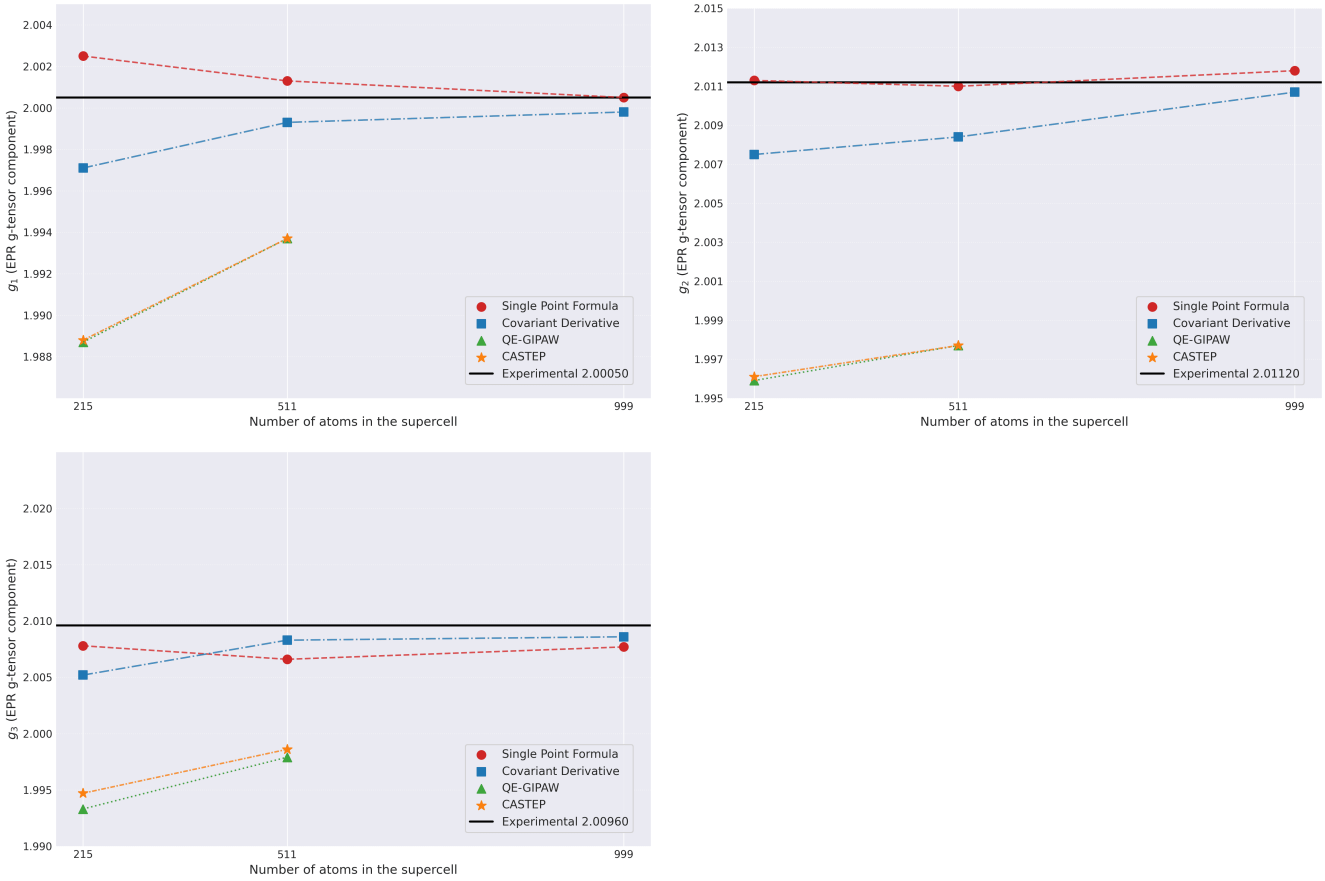

FIG. 1. Computed g-tensor components for the E-center (PV^0) in silicon as a function of supercell size, using only the Γ-point. Results from QE-CONVERSE with the covariant approach (blue squares) and the single-point formula (red circles) are compared with QE-GIPAW (green triangles) and CASTEP (yellow stars).

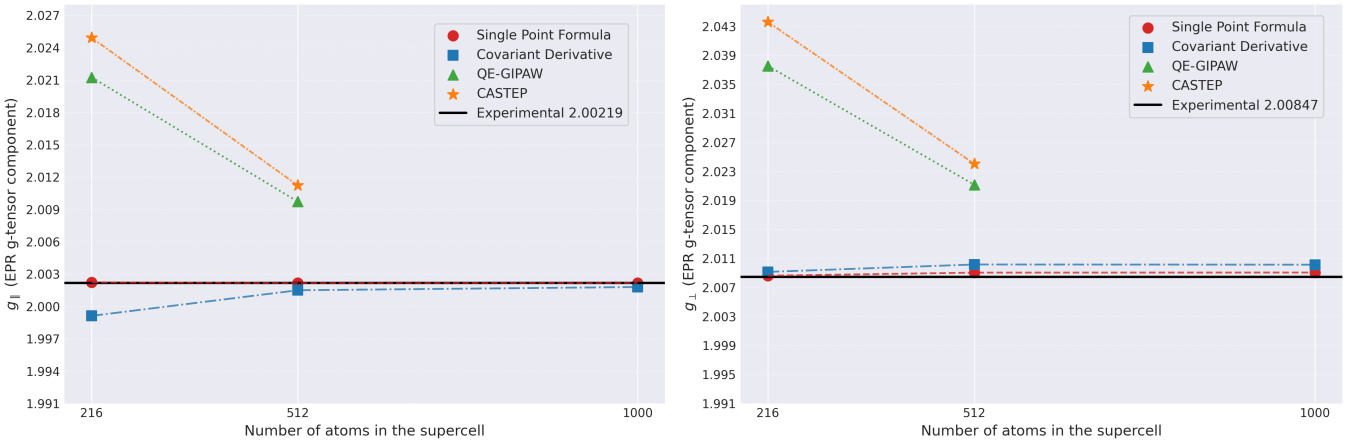

FIG. 2. Computed g-tensor components for the substitutional nitrogen defect (N_{Si}) in silicon in its off-center configuration, using Γ-point sampling and increasing supercell size. QE-CONVERSE results obtained via the covariant method (blue squares) and the single-point formula (red circles) are shown alongside linear response results from QE-GIPAW (green triangles) and CASTEP (yellow stars).

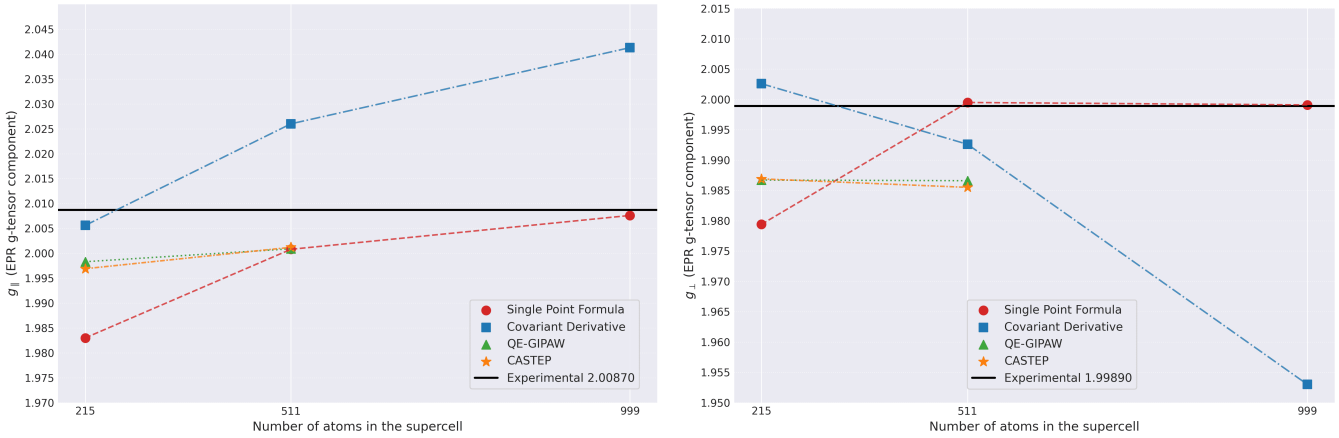

FIG. 3. Computed g-tensor components for the positively charged (V^+) in silicon as a function of supercell size, using only the Γ-point. Results from QE-CONVERSE with the covariant approach (blue squares) and the single-point formula (red circles) are compared with QE-GIPAW (green triangles) and CASTEP (yellow stars).

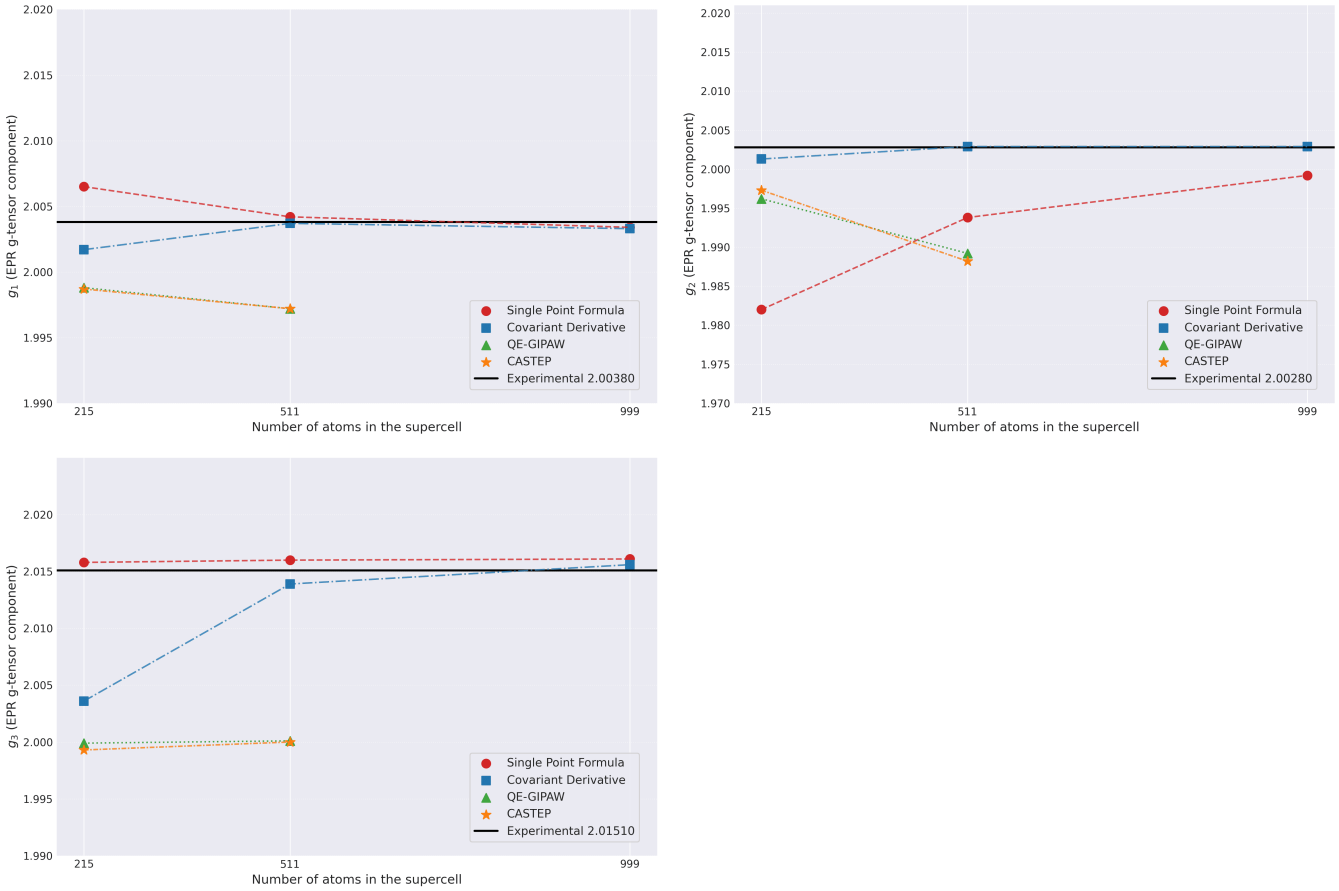

FIG. 4. Computed g-tensor components for the negative monovacancy (V^-) in silicon as a function of supercell size, using only the Γ-point. Results from QE-CONVERSE with the covariant approach (blue squares) and the single-point formula (red circles) are compared with QE-GIPAW (green triangles) and CASTEP (yellow stars).

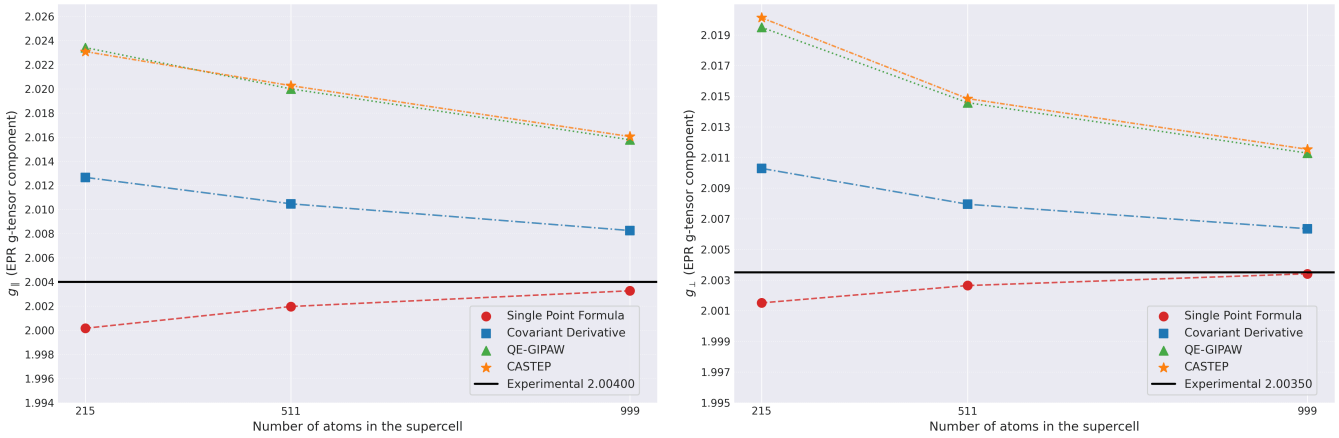

FIG. 5. Computed g-tensor components for the SiV^0 defect in diamond as a function of supercell size, using only the Γ-point. Results from QE-CONVERSE with the covariant approach (blue squares) and the single-point formula (red circles) are compared with QE-GIPAW (green triangles) and CASTEP (yellow stars).

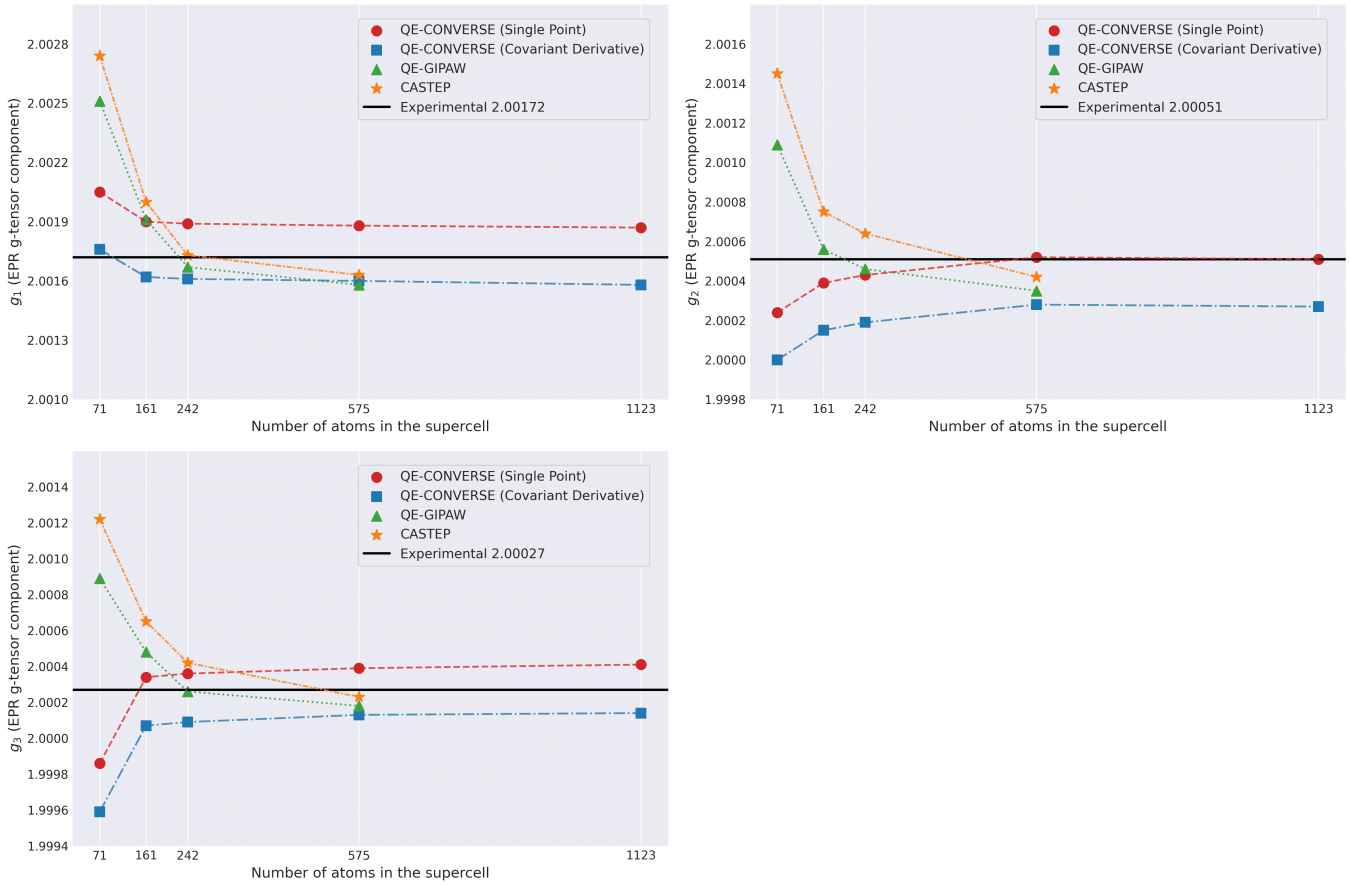

FIG. 6. Computed g-tensor components for the E_1' center in α-quartz, as representative of E′ centers in silica, as a function of supercell size, using only the Γ-point. Results from QE-CONVERSE with the covariant approach (blue squares) and the single-point formula (red circles) are compared with QE-GIPAW (green triangles) and CASTEP (yellow stars).

Hyperfine parameters of the V^+ and V^- defects in silicon

Hyperfine Site	A_1 (MHz)	A_2 (MHz)	A_3 (MHz)	A_{iso}	A_{aniso}	α^2	β^2	η^2
Si (x4)	127.1	84.5	86.5	99.4	14.8	0.14	0.86	17.2%
Si (x4) Exp.[3]	131.6	89.3	89.3	103.4	14.1	0.15	0.85	16.5%

TABLE VII. Calculated and experimental hyperfine parameters for the four equivalent silicon atoms surrounding the V^+ defect in silicon. Listed are the principal values of the hyperfine tensor (A_1, A_2, A_3), the isotropic and anisotropic contributions $(A_{\mathrm{iso}}, A_{\mathrm{aniso}})$, and the spin–population coefficients $(\alpha^2, \beta^2, \eta^2)$.

Hyperfine Site	A_1 (MHz)	A_2 (MHz)	A_3 (MHz)	A_{iso}	A_{aniso}	α^2	β^2	η^2
Si (x2)	391.7	332.7	329.3	351.2	20.2	0.30	0.70	25.6%
Si (x2) Exp.[4]	400.4	332.3	334.8	355.8	22.3	0.28	0.72	27.7%

TABLE VIII. Calculated and experimental hyperfine parameters for the two equivalent silicon atoms surrounding the V^- defect in silicon. Listed are the principal values of the hyperfine tensor (A_1, A_2, A_3), the isotropic and anisotropic contributions $(A_{\mathrm{iso}}, A_{\mathrm{aniso}})$, and the spin–population coefficients $(\alpha^2, \beta^2, \eta^2)$.

The hyperfine interactions of the silicon monovacancy in its two charge states, V^+ and V^-, provide direct insight into the spatial distribution and orbital character of the unpaired electron associated with each defect configuration.

For the positively charged vacancy V^+, the unpaired spin is distributed over the four silicon atoms surrounding the monovacancy. As reported in Table VII, the calculated hyperfine tensor components (A_1, A_2, A_3) show excellent agreement with experiment. From the isotropic and anisotropic contributions, the extracted spin–population coefficients reveal that each silicon atom carries approximately 17.2% of the total spin density, in close correspondence with the experimental value of 16.5%. The wavefunction exhibits a predominantly p-like character, with $\beta^2 = 0.86$.

In the negatively charged vacancy V^-, the defect undergoes a rebonding distortion along the $\langle 011 \rangle$ direction, resulting in two equivalent silicon atoms that dominate the hyperfine response. The values listed in Table VIII demonstrate excellent agreement between the calculated and experimental hyperfine tensors. The spin–population analysis indicates that each of the two silicon atoms hosts about 25.6% of the total unpaired electron density (experimental value 27.7%). The spin density again shows a mixed sp-like character, with a dominant p-component ($\beta^2 = 0.70$).

HYPERFINE PARAMETERS: DEFINITIONS AND ANALYTICAL EXPRESSIONS

The hyperfine interaction between the unpaired electron and the surrounding ^{29}Si nuclear spins was analyzed by decomposing the hyperfine tensor of each inequivalent silicon site i into its isotropic (Fermi contact) and anisotropic (dipolar) components:

$$A_i = A_{\mathrm{iso},i} + A_{\mathrm{aniso},i}.$$

The analytical expressions used follow the standard Watkins–Corbett treatment for point defects in silicon, where the unpaired-electron wavefunction at each site is expressed in terms of its s- and p-like components, with spin population coefficients α_i^2 and β_i^2. The quantity η_i^2 denotes the total spin population localized on site i.

Isotropic (Fermi Contact) Contribution

The Fermi-contact interaction arises from the s-like part of the wavefunction and is expressed as:

$$A_{\mathrm{iso},i} = \frac{8\pi}{3} g_e \mu_B \frac{\mu_{I_i}}{I_i} \left|\psi_{s,i}(0)\right|^2 \alpha_i^2 \eta_i^2, \tag{1}$$

Here:

- g_e is the free-electron g-factor ($g_e = 2.002319$),
- μ_B is the Bohr magneton,
- μ_{I_i} is the nuclear magnetic moment of the i-th nucleus,
- I_i is the nuclear spin quantum number of that nucleus ($I = 1/2$ for ^{29}Si),
- $|\psi_{s,i}(0)|^2$ is the electron contact density at the nucleus for an s-type orbital.

paramagnetic resonance studies

Anisotropic (Dipolar) Contribution

The anisotropic hyperfine term originates from the p-like component of the spin density and is given by:

$$A_{\mathrm{aniso},i} = \frac{2}{5} g_e \mu_B \frac{\mu_{I_i}}{I_i} \langle r_{p,i}^{-3} \rangle \beta_i^2 \eta_i^2, \tag{2}$$

where $\langle r_{p,i}^{-3} \rangle$ is the radial expectation value associated with the dipolar field generated by a p-type orbital.

Atomic Parameters

The quantities $|\psi(0)|^2$ and $\langle r^{-3} \rangle$ are atomic parameters for silicon obtained from **Hartree–Fock calculations of the 3s and 3p valence orbitals**. These values were originally tabulated by Watkins and Corbett in Ref. [1]) and remain the standard reference for extracting hyperfine population coefficients in Si-based point defects. Table .

Atom	$\lvert\psi(0)\rvert^2$ ($10^{24}\,\mathrm{cm}^{-3}$)	$\langle r^{-3} \rangle$ ($10^{24}\,\mathrm{cm}^{-3}$)
Si (3s, 3p HF)	31.5	16.1

GEOMETRICAL ORIGIN OF ORBITAL MAGNETIZATION AND THE LARGE-SUPERCELL LIMIT

Berry phase as a geometric phase

In crystalline solids with periodic boundary conditions, the electronic states can be written in Bloch form,

$$\psi_{n\mathbf{k}}(\mathbf{r}) = e^{i\mathbf{k}\cdot\mathbf{r}}\, u_{n\mathbf{k}}(\mathbf{r}),$$

where $u_{n\mathbf{k}}(\mathbf{r})$ has the periodicity of the lattice and n labels the band index. The central object of Berry-phase theory is the *Berry connection* [7] of band n,

$$\mathbf{A}_n(\mathbf{k}) = i \left\langle u_{n\mathbf{k}} \middle| \nabla_{\mathbf{k}} u_{n\mathbf{k}} \right\rangle,$$

which plays the role of a gauge field in reciprocal space.

Given a closed loop $\mathcal{C}$ in the Brillouin zone (BZ), the associated Berry phase [8] of band n is defined as

$$\gamma_n[\mathcal{C}] = \oint_{\mathcal{C}} \mathbf{A}_n(\mathbf{k}) \cdot d\mathbf{k}.$$

This phase is *geometric* in the sense of Berry: it depends only on the path traced by the projector onto the occupied manifold along $\mathcal{C}$, and not on the dynamical phase or on the parametrization of the loop. Under smooth gauge transformations $u_{n\mathbf{k}} \to e^{i\phi_n(\mathbf{k})} u_{n\mathbf{k}}$, the Berry connection changes by a gradient, $\mathbf{A}_n \to \mathbf{A}_n + \nabla_{\mathbf{k}} \phi_n$, so that the Berry phase $\gamma_n[\mathcal{C}]$ is well defined modulo 2π, i.e. modulo a "quantum" of phase.

Berry connection, Brillouin-zone topology, and orbital magnetization

In periodic boundary conditions, the Brillouin zone is a compact manifold where opposite faces are identified; topologically it is a three-dimensional torus, $\mathrm{BZ} \sim T^3$. A loop $\mathcal{C}$ defined by integrating $\mathbf{k}$ along one reciprocal-lattice direction therefore closes on itself by construction: $\mathbf{k}$ and $\mathbf{k}+\mathbf{G}$ represent the same physical state.

The Berry connection and its curl, the Berry curvature [9]

$$\mathbf{\Omega}_n(\mathbf{k}) = \nabla_{\mathbf{k}} \times \mathbf{A}_n(\mathbf{k}),$$

enter directly the modern theory of polarization and orbital magnetization [10].

Orbital magnetization in the modern theory: local and itinerant contributions

In the modern theory of orbital magnetization, the total orbital magnetization is decomposed into two distinct geometric contributions [10–13]:

$$M_{\mathrm{orb}} = M_{\mathrm{LC}} + M_{\mathrm{IC}}.$$

(i) Local circulation (LC). M_{LC} describes the internal self-rotation of the electronic wave packet within a unit cell. Physically, it corresponds to the "local circulation" of Wannier functions: the electron behaves as a small current loop centered around the lattice site. Mathematically, it is expressed as a geometric quantity involving a generalized curvature weighted by the Hamiltonian,

$$M_{\mathrm{LC}} \;\propto\; \mathrm{Im} \sum_n^{\mathrm{occ}} \int_{\mathrm{BZ}} \frac{d^3k}{(2\pi)^3} \left\langle \partial_{\mathbf{k}} u_{n\mathbf{k}} \right| H(\mathbf{k}) - \varepsilon_{n\mathbf{k}} \left| \partial_{\mathbf{k}} u_{n\mathbf{k}} \right\rangle,$$

In semiclassical language, this term is directly related to the semiclassical formula for the magnetizatioin of a wavepacket in the n-th band [14].

(ii) Itinerant circulation (IC). M_{IC} accounts for the motion of the center of mass of electronic wave packets as they propagate through the crystal. This contribution reflects the geometric deflection (anomalous velocity) induced by the Berry curvature, and is responsible for surface currents in finite samples. It is given by

$$M_{\mathrm{IC}} \;\propto\; \sum_n^{\mathrm{occ}} \int_{\mathrm{BZ}} \frac{d^3k}{(2\pi)^3} \; (\varepsilon_{n\mathbf{k}} - \mu)\; \mathbf{\Omega}_n(\mathbf{k}).$$

making explicit that the Berry curvature enters the orbital magnetization through the itinerant circulation term. Since these contributions are constructed entirely from gauge-invariant geometric quantities-such as the Berry curvature and the projectors onto the occupied manifold—the total orbital magnetization is a geometric observable.

Discretization of the Berry connection and the $L \to \infty$ limit

Following Resta [15], we start from the Berry connection of the n-th occupied band,

$$A_x(\mathbf{k}) = i \langle u_{n\mathbf{k}} \mid \partial_{k_x} u_{n\mathbf{k}} \rangle.$$

Because the periodic parts $u_{n\mathbf{k}}$ obtained from numerical diagonalization carry an arbitrary $\mathbf{k}$–dependent phase, the derivative cannot be evaluated directly. One therefore introduces the overlap matrix

$$S_{jj'}(\mathbf{k}, \mathbf{k}') = \langle u_{j\mathbf{k}} \mid u_{j'\mathbf{k}'} \rangle,$$

which is gauge covariant but becomes gauge invariant when used inside traces or determinants. The Berry connection is then rewritten as

$$A_x(\mathbf{k}) = i \; \frac{\partial}{\partial k'_x} \operatorname{tr} S(\mathbf{k}, \mathbf{k}') \Big|_{\mathbf{k}'=\mathbf{k}} = i \; \frac{d}{dq} \operatorname{tr} S(\mathbf{k}, \mathbf{k} + q\mathbf{e}_x) \Big|_{q=0},$$

and using the identity $\operatorname{tr}(S^{-1}\partial_k S) = \partial_k \ln \det S$,

$$A_x(\mathbf{k}) = -\; \frac{d}{dq} \, \mathrm{Im} \, \ln \det S\big(\mathbf{k}, \mathbf{k} + q\mathbf{e}_x\big) \Big|_{q=0}.$$

Discretized connection. On a regular mesh $k_m = 2\pi m/(Ma)$, the derivative is approximated as a finite difference:

$$A_x(k_m) \simeq -\frac{Ma}{2\pi}\,\mathrm{Im}\,\ln\det S(k_m, k_{m+1}), \qquad k_M \equiv k_0.$$

Discretized Berry phase. The Berry phase over the loop $0 \to 2\pi/a$ is then

$$\gamma_x = \int_0^{2\pi/a} dk_x\, A_x(k_x) \simeq \sum_{m=0}^{M-1} \mathrm{Im}\,\ln\det S(k_m, k_{m+1}).$$

Single-point limit. In a supercell of length $L = Ma$, the Brillouin zone shrinks to the interval $[0, 2\pi/L]$, and the k-point spacing is

$$\Delta k = \frac{2\pi}{L}.$$

In the limit $L \to \infty$, i.e. $\Delta k \to 0$, the Brillouin-zone loop contracts to a single point. The discretized phase associated with a step $k \to k + \Delta k$ is

$$\mathrm{Im}\,\ln\det S(k, k + \Delta k),$$

and its small–Δk behaviour follows from

$$S(k, k + \Delta k) = \langle u_k | u_{k+\Delta k} \rangle \simeq 1 + i\, A_x(k)\, \Delta k,$$

where $A_x(k)$ is the Berry connection. Using $\ln(1 + z) \simeq z$ for $|z| \ll 1$,

$$\ln\det S(k, k + \Delta k) \simeq i\, A_x(k)\, \Delta k,$$

so that

$$\mathrm{Im}\,\ln\det S(k, k + \Delta k) \simeq A_x(k)\, \Delta k.$$

The discretized phase therefore vanishes linearly with Δk.

In Berry-phase observables (such as the electronic polarization [10]), this phase always appears in the combination

$$P_x \propto \frac{1}{\Delta k}\,\mathrm{Im}\,\ln\det S(k, k + \Delta k)[15].$$

Substituting the above expansion gives

$$P_x \propto \frac{1}{\Delta k}\left[A_x(k)\, \Delta k\right] = A_x(k),$$

which remains finite and well defined in the limit $\Delta k \to 0$.

Thus, although the loop in k-space shrinks to zero length in the thermodynamic limit, the geometric phase retains a well-defined physical meaning.

Since the Berry phase remains well defined in the $L \to \infty$ limit, its k-space derivatives—the Berry connection and Berry curvature—also retain their physical meaning. The modern theory of orbital magnetization is constructed entirely from such geometric quantities (Berry curvature, orbital moments, and projectors). Consequently, M_{orb} admits a discretized formulation that remains valid as the k-mesh is coarsened. In a large supercell where $\Delta k \to 0$, all geometric ingredients entering M_{orb} remain well defined even when evaluated at a single k-point. This provides a rigorous foundation for evaluating the converse g-tensor at Γ in sufficiently large supercells, in direct analogy with the single-point Berry phase approach for polarization.

References for this section

* sfioccola@laas.fr

[1] G. D. Watkins and J. W. Corbett. Defects in Irradiated Silicon: Electron Paramagnetic Resonance and Electron-Nuclear Double Resonance of the Si- E Center. *Phys. Rev.*, 134(5A):A1359–A1377, June 1964.

[2] M. Belli, M. Fanciulli, and D. Batani. Electron spin resonance of substitutional nitrogen in silicon. *Phys. Rev. B*, 89(11):115207, March 2014.

[3] G D Watkins. An epr study of the lattice vacancy in silicon. *J. Phys. Soc. Japan*, Vol: 18: Suppl. II, 03 1963.

[4] M. Sprenger, S. H. Muller, E. G. Sieverts, and C. A. J. Ammerlaan. Vacancy in silicon: Hyperfine interactions from electron-nuclear double resonance measurements. *Phys. Rev. B*, 35:1566–1581, Feb 1987.

[5] A. M. Edmonds, M. E. Newton, P. M. Martineau, D. J. Twitchen, and S. D. Williams. Electron paramagnetic resonance studies of silicon-related defects in diamond. *Phys. Rev. B*, 77:245205, Jun 2008.

[6] B D Perlson and J A Weil. Electron paramagnetic resonance studies of the e' centers in alpha-quartz. *Can. J. Phys.*, 86(7):871–881, 2008.

[7] G Papadopoulos. A generalization of berry's connection. *Journal of Physics A: Mathematical and General*, 25(7):2071, apr 1992.

[8] Michael Victor Berry. Quantal phase factors accompanying adiabatic changes. *Proceedings of the Royal Society of London. A. Mathematical and Physical Sciences*, 392(1802):45–57, 1984.

[9] Nico Sprinkart, Elke Scheer, and Angelo Di Bernardo. Tutorial: From topology to hall effects—implications of berry phase physics. *Journal of Low Temperature Physics*, 217(5):686–719, Dec 2024.

[10] Raffaele Resta. Electrical polarization and orbital magnetization: the modern theories. *J. Phys.: Condens. Matter*, 22(12):123201, March 2010.

[11] Davide Ceresoli, T. Thonhauser, David Vanderbilt, and R. Resta. Orbital magnetization in crystalline solids: Multi-band insulators, Chern insulators, and metals. *Phys. Rev. B*, 74(2):024408, July 2006.

[12] T. Thonhauser, Davide Ceresoli, David Vanderbilt, and R. Resta. Orbital Magnetization in Periodic Insulators. *Phys. Rev. Lett.*, 95(13):137205, September 2005.

[13] Davide Ceresoli and Raffaele Resta. Orbital magnetization and Chern number in a supercell framework: Single k -point formula. *Phys. Rev. B*, 76(1):012405, July 2007.

[14] Ganesh Sundaram and Qian Niu. Wave-packet dynamics in slowly perturbed crystals: Gradient corrections and berry-phase effects. *Phys. Rev. B*, 59:14915–14925, Jun 1999.

[15] Raffaele Resta. The single-point berry phase in condensed-matter physics. *Journal of Physics A: Mathematical and Theoretical*, 55(49):491001, dec 2022.